5. Double Circular Arc (DCA) cascade blade flow, problem statement

The second test case deals with a DCA compressor cascade, which is considered a severe challenge for the CFD codes, due to the presence of large transition and separation phenomena arising along highly curved blade surfaces even at near-design conditions has shown by the experimental work carried out by Zierke and Deutsch (1989). From this point of view, the HRN simulations carried are able to describe approximately the flow physics in proximity of blade profile. Nevertheless, several key features and benefits of the implemented algebraic non-linear models against the standard one are here issued.

Geometrical description of the flow

The present test case studies the flow physics developing around a highly loaded compressor blade in cascade at slight off-design incidence. The flow is two-dimensional with constant temperature, and could be considered virtually incompressible.

The geometry of one pitch of the cascade with double-circular-arc profile blade is shown in Fig. 17. The cascade geometrical characteristic are here resumed:

- blade pitch: t = 106.8 mm
- camber-line curvature radius: 212.8 mm
- camber angle: $\theta = 65^{o}$
- stagger angle: $\gamma = 20.5^{o}$
- blade solidity: $\sigma = 2.14$
- chord length: c or l_c = 228.6 mm
- leading and the trailing edges curvature radius: 0.9144 mm

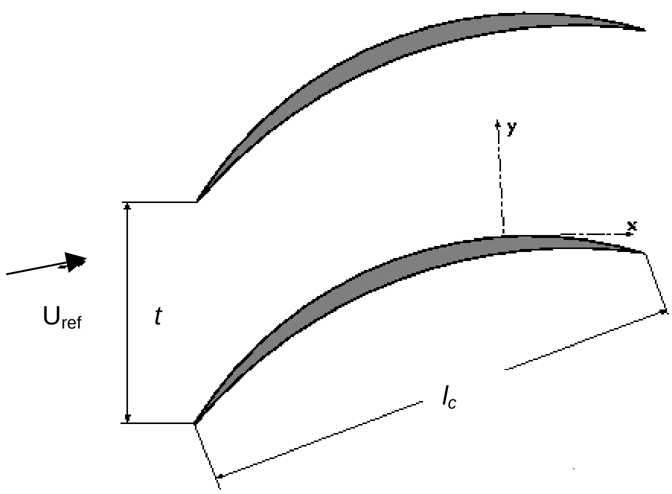

Fig. 17: DCA cascade geometry

Flow parameters and inflow conditions

Air with a kinematic viscosity $\nu = 1.5 \times 10^{-5}$m^2/s and a density ρ = 1.205 kg/m^3. Inlet mean velocity: U_{ref} = 33 m/s. The Reynolds number is based on the chord lenght: $Re_c = U_{ref}c/\nu = 5.01 \times 10^5$. The inlet Mach number is Ma_i = 0.1. The adopted incidence angle has been imposed to the inlet flow: -1.5°.

At the inlet section of the test-rig a constant mean velocity profile is obtained and turbulent quantity levels compatible with a free-stream turbulence level of 0.18%.

5.1 DCA cascade numerical model

Algebraic turbulence model & numerical scheme

The present investigation is carried out by using the explicit algebraic Reynolds stress model proposed by Gatski and Speziale (1993), labeled as GS93, implemented within a k-ε formulation. The derivation of the algebraic formulation for the Reynolds stress is based on the isotropic dissipation rate hypothesis, and on the linearization of the Reynolds stress equation about the equilibrium value of the production-to-dissipation ratio (see **part 1 section 2.1**).

The numerical campaigns have been carried out using the numerical scheme outlined in **part 1 section 3**. The convergence threshold has been set equal to 10^{-4} for both the solution errors and its residual.

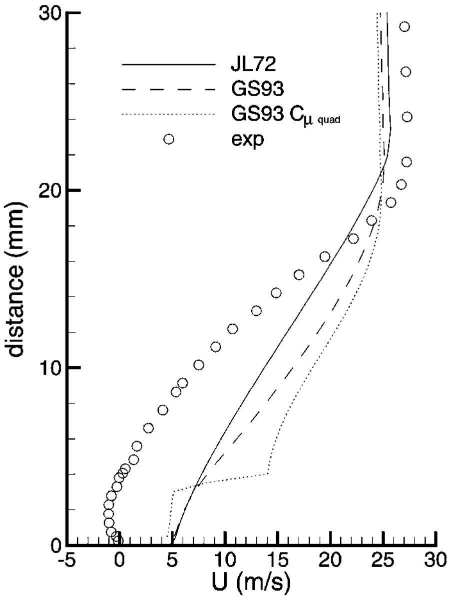

Fig. 18: Velocity profiles on SS @ 90.3% chord

Remarks: During the numerical studies, a modification was introduced in the GS93 model implementation. The reason for this intervention could be discussed with reference to the boundary layer behavior on blade suction side in the separation region. To this end, in Fig. 18 are plotted the stream-wise velocity profiles at 90.3% of chord within the boundary layer separation core. The experimental data are compared to the following predictions: linear eddy-viscosity *k*-*ε* model JL72 (Jones and Launder, 1972); explicit algebraic Gatski and Speziale (1993) model implemented with a quadratic element-wise interpolation for the effective viscosity, labeled as GS93 $C_{\mu quad}$; explicit algebraic Gatski and Speziale (1993) model implemented with a constant element-wise interpolation for the effective viscosity, simply labeled as GS93. It is important to note that the GS93 $C_{\mu quad}$ profile shows and evident discontinuity that on the authors opinion is consequent to the non-equilibrium sensitivity that the model preserves, although its HRN implementation, by means of the effective viscosity dependence form strain and vorticity invariants.

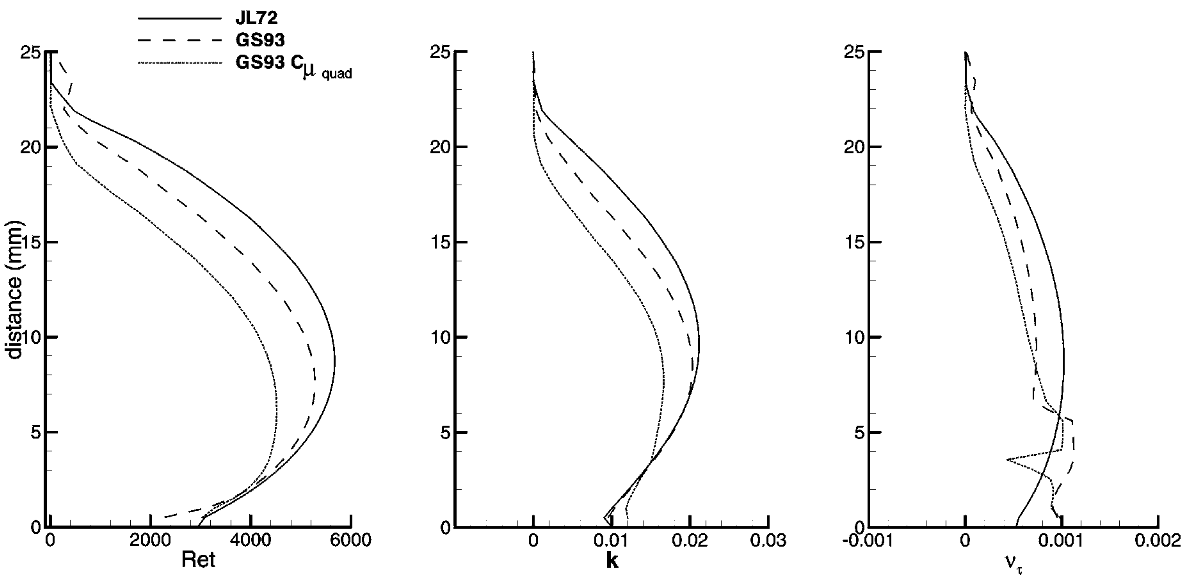

Fig. 19: Turbulent quantities profiles on SS @ 90.3% chord
a.) Re_t, b.) k, c.) ν_t

This idea is supported by the analysis of the distributions, within the boundary layer at the same chord-wise section, of the following turbulent quantities: turbulent Reynolds number $Re_t = k^2 / \nu\, \varepsilon$ (Fig. 19.a), turbulent kinetic energy k (Fig. 19.b), the eddy-effective viscosity ν_t, $\nu_t^{eff} = C_\mu^{eff}\, k^2/\varepsilon$ (Fig. 19.c). In Fig. 19.c, clearly appears that the velocity discontinuity is related to the collapse of effective viscosity profile, in response to a possible production-to-dissipation ratio peak. Whereas all the other probed quantities are not affected by discontinuities. The solution proposed and applied consists in the degradation of the interpolation order of the effective viscosity (from quadratic to element-wise constant), in order to reduce its spatial non-linear dependence. As clearly demonstrated by both Fig. 18 and Fig. 19.a – 19.c, the instability is recovered preserving the prediction consistency.

Computational domain description

A combined H-O topology was used to model the flow region, the mesh consists of 55224 nodes and is aligned respectively with theoretical inlet and outlet flow directions. In the vicinity of the blade profile (O-topology region) 60 nodes are used normal to the blade surface. Figure 20 shows grid details around the blade leading and trailing edges. The grid refinement towards blade surface controls the dimensionless distance y^+ value about 30 on the first nodes row.

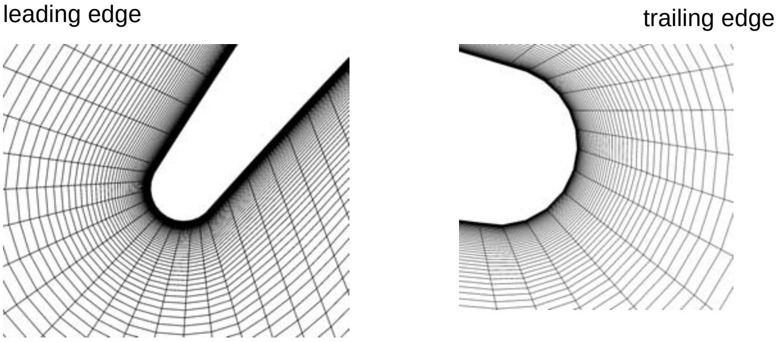

Fig. 20: Grid detail near leading and trailing edges

Boundary conditions

At the inlet section of the computational domain (set one chord upstream the blade leading edges), the constant experimental mean velocity profile is used. The inlet turbulence intensity and length scale, used to model the inlet profile of k and ε, are based on the values recommended by Chen et al. (1998): TI = 2%, l_ε = 1.9% of blade chord. These values are applied half-chord upstream the blade and they are compatible with the turbulence level measured at the edge of blade boundary layers.
The solid boundaries are treated with the wall-function, using the WFN model (see **part 1 section 4.1**) which does not fail in the simulation of regions where the flow stagnates or separates.

5.2 DCA cascade blade flow, results and discussion

Blade boundary layer data

The blade boundary layers have been investigated on six measurement sections, respectively: 19.7 %, 49.7% and 90.3 % of blade chord on suction side (SS); 20.7%, 55.1 % and 89.7% of blade chord on pressure side (PS). The comparative investigation involves the mean velocities, and turbulent quantities behavior around the blade surfaces.
In Fig. 21 and Fig. 22 respectively, the computed distributions of displacement thickness δ and boundary layer shape factor H are plotted against the measured ones for the blade SS. It is remarkable to note the agreement of HRN predictions to the experiments in simulating δ behavior, up to the chordwise location where the separation starts. Concerning the numerics, the JL72 data seem to outperform the GS93 one in particular in the separation region.
In Fig. 23 to 25, is investigated the behavior of predicted boundary layer on blade PS respectively at 20.7%, 55.1 % and 89.7% of blade chord. Both the predictions resolve similarly the boundary layer flow fields, and are affected by a marked under-estimation of physical shear stress at the wall. This is because on blade pressure side laminar effects, that could not be simulated with a HRN approach, dominate the boundary layer development.
In Fig. 26 to 28, is investigated the behavior of predicted boundary layer on blade SS respectively at 19.7%, 49.7 % and 90.3% of blade chord. On blade suction side, where the boundary layer is turbulent as shown by Fig. 22, the JL72 and GS93 prediction agree qualitatively to the measured

velocity distributions also in the vicinity of the wall. Clearly no separation is predicted, although the GS93 profile at 90.3% of chord tends to behave closer to the measured one in terms of profile slope distribution.

Fig. 29 shows the Re_t profiles developing along the blade suction side within the attached region (up to 60% of chord). The two models are both able of predicting the boundary layer development in closer quantitative similarity. The only exception to be highlighted, is that GS93 tends to predict also the turbulence decrease approaching the wall region. In Fig. 30, the predicted turbulence intensity *TI* profiles are compared to the experiments in the suction separation core at 90.3% of chord. The comparison shows that, in the limit of the used HRN approach, the turbulence level is correctly predicted in terms of its maximum as well as its variation.

Static pressure coefficient

In Fig. 31 the static pressure coefficient distribution are shown. The following comments could be drawn. On SS, both the models are able of predicting the physical deceleration at the leading edge, clearly confirming the high quality of the used discretization. Although the subsequent acceleration is over-predicted. This probably causes also the adverse pressure gradient to be less steeper than experiments up to mid-chord than invalidating the chance of predicting boundary layer separation. On PS, both the models over-predict the flow acceleration about the leading edge. As a consequence, along the blade surface they simulate higher adverse pressure gradient. It is worth to note that at the trailing edge the GS93 is able to recover the experimental behavior predicting the correct flow acceleration.

Turbulent kinetic energy profiles around blade leading edge

The Fig.s 32, and 33 show the turbulence intensity field in the vicinity of the blade leading edge. In detail, Fig. 32 shows both the Re_t and *TI* distributions evaluated along the stagnating streamlines from 1 mm distance to the blade leading edge. It is worth to note that the GS93 model is able of controlling the growth of turbulence intensity about the leading edge in the region where the flow stagnates. Although the HRN regime, it is thus expected that the algebraic non-linear model could alleviate the effect of the so-called stagnation anomaly which is typical of linear closure such as JL72.

References

Chen, W.L., Lien, F. and Leschziner, M.A., Computational prediction of flow around highly-loaded compressor cascade blade with non-linear eddy-viscosity model, *Int. J. of Heat Fluid Flow*, **19**, 1998, 307-319.

Chen, W.L., and Leschziner, M.A., Modeling turbomachine-blade flows with non-linear eddy-viscosity models and second moment closure, IMechE Paper C557/131/99, 1999, **A**, 189-199.

Gatski, B.T., and Speziale, C. G., On explicit algebraic stress models for complex turbulent flows, *J. Fluid Mech.*, **254**, 1993, 59-78.

Jones, W.P., and Launder, B.E., The prediction of laminarization with a two-equation model of turbulence, *Int. J. of Heat Mass Transfer*, **15**, 1972, 301-314.

Zierke, W.C., and Deutsch, S., The measurement of boundary layers on a compressor blade in cascade, Vols. 1 and 2, NASA CR 185118, 1989.

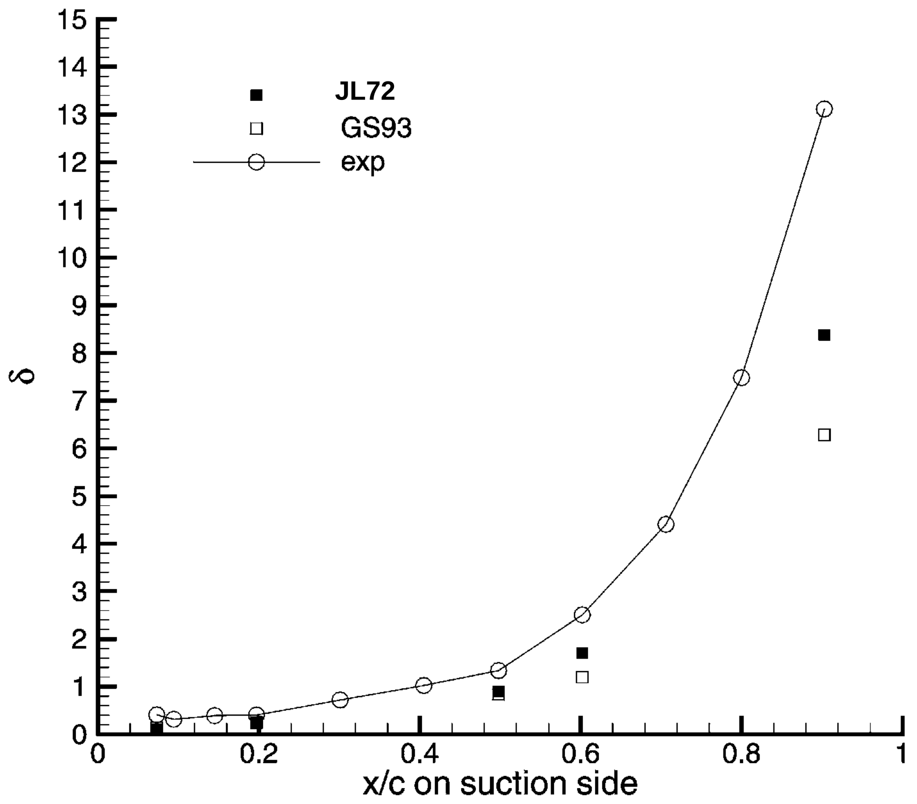

Fig. 21: Suction side blade boundary layer, chordwise displacement thickness distribution

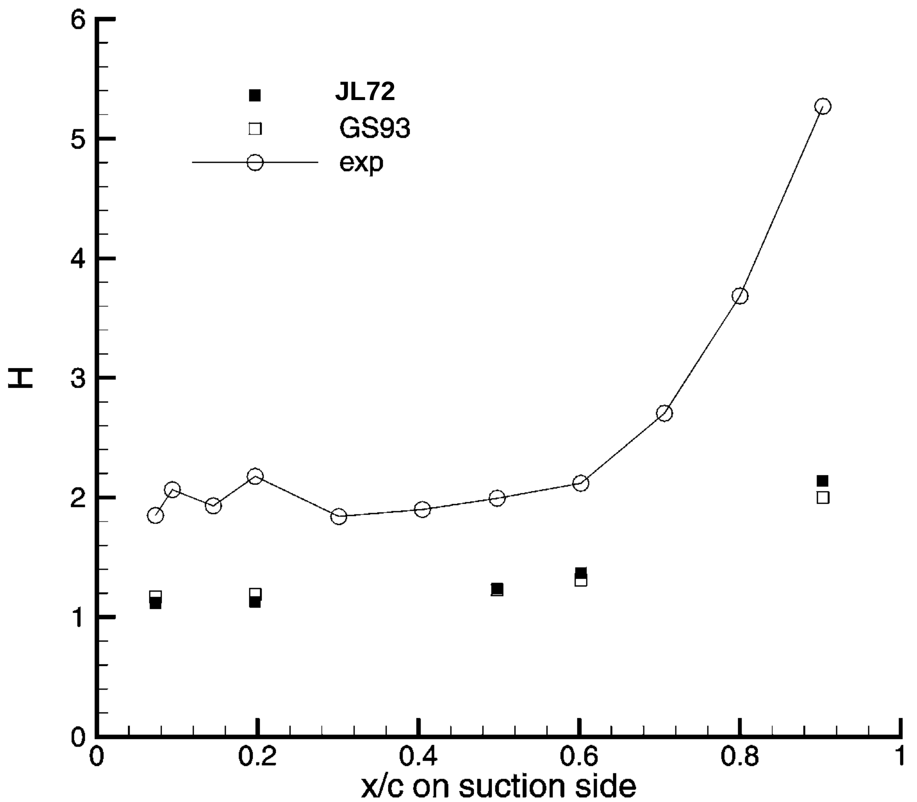

Fig. 22: Suction side blade boundary layer, chordwise shape factor distribution

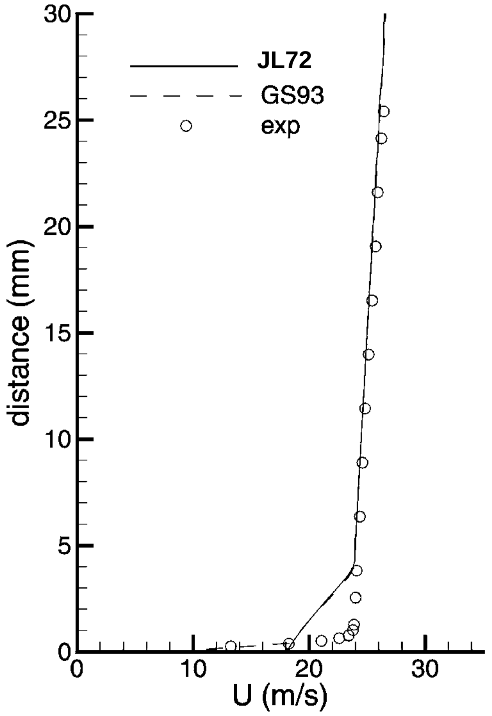

Fig. 23: Pressure side blade boundary layer velocity profile (@ 20.7% of the chord)

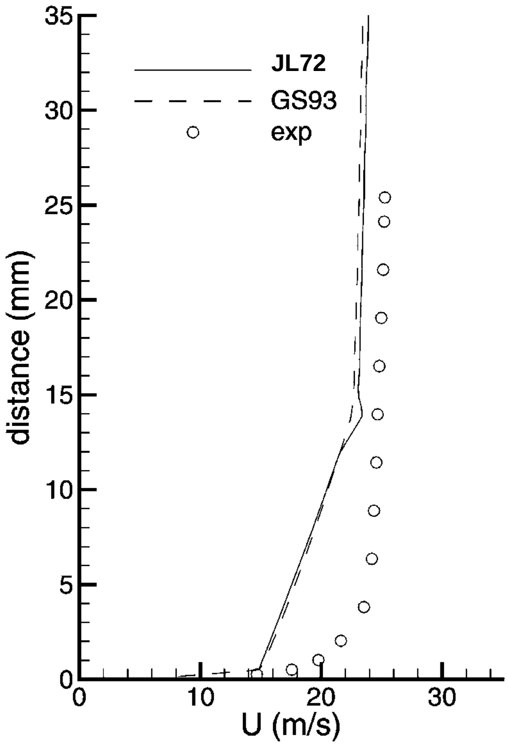

Fig. 24: Pressure side blade boundary layer velocity profile (@ 55.1% of the chord)

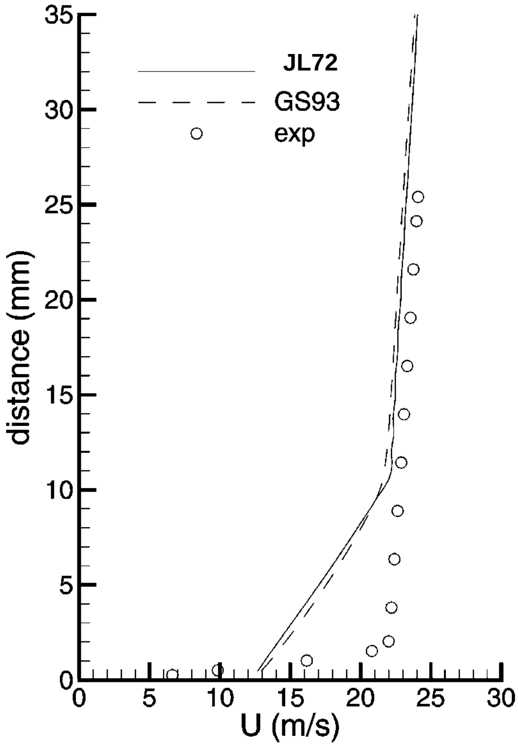

Fig. 25: Pressure side blade boundary layer velocity profile (@ 89.7% of the chord)

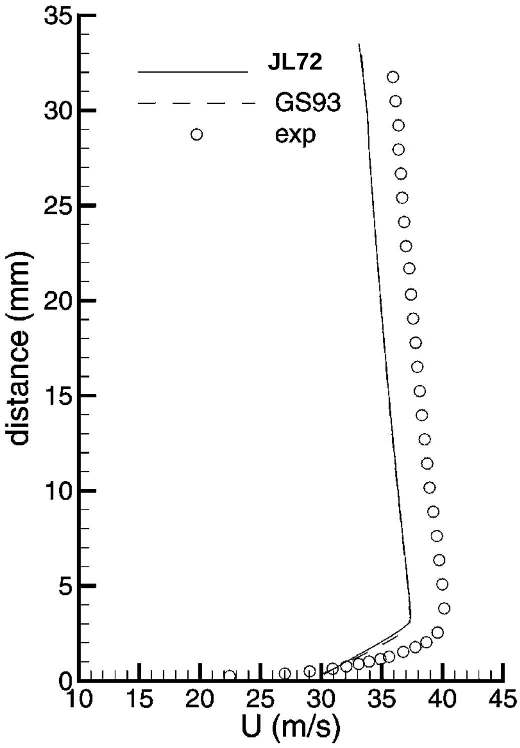

Fig. 26: Suction side blade boundary layer velocity profile (@ 19.7% of the chord)

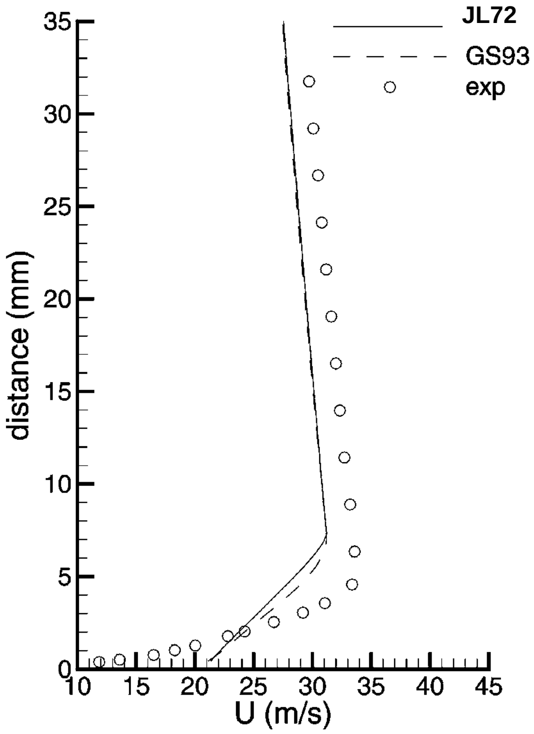

Fig. 27: Suction side blade boundary layer velocity profile (@ 49.7% of the chord)

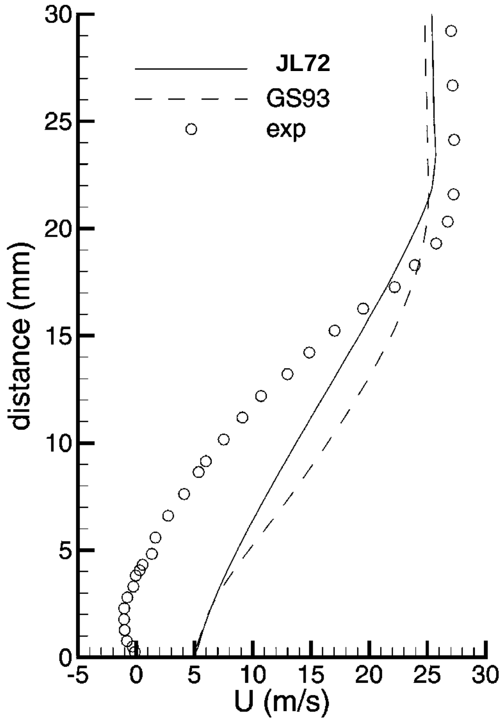

Fig. 28: Suction side blade boundary layer velocity profile (@ 90.3% of the chord)

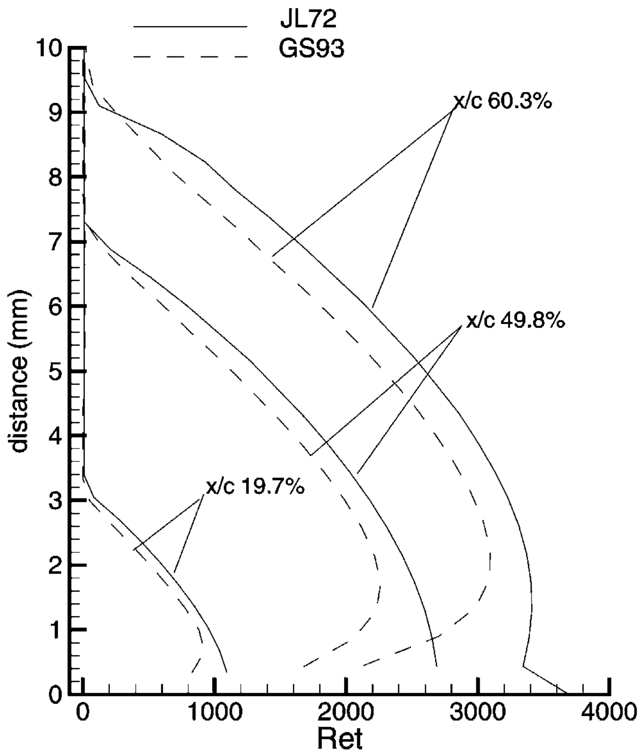

Fig. 29: Suction side blade boundary layer Re_t distribution along the chord

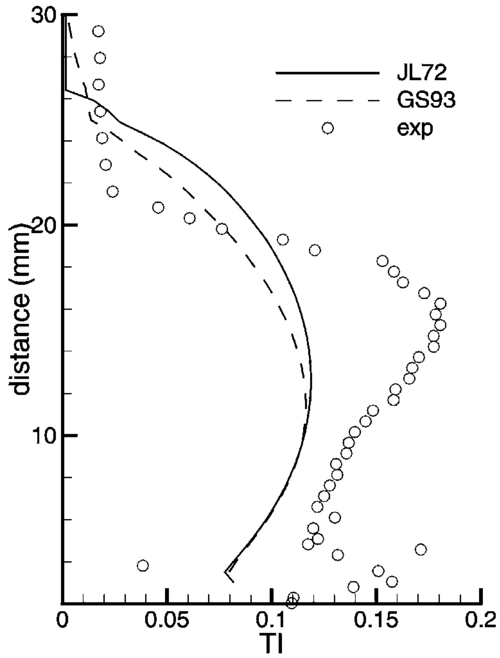

Fig. 30: Suction side blade boundary layer turbulence intensity *TI* profile (@ 90.3% of the chord)

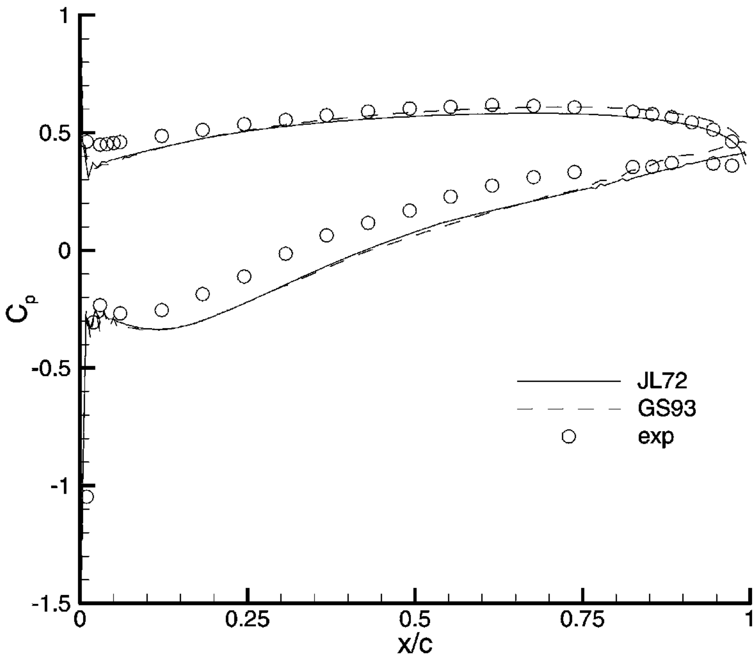

Fig. 31: Static pressure coefficient distribution

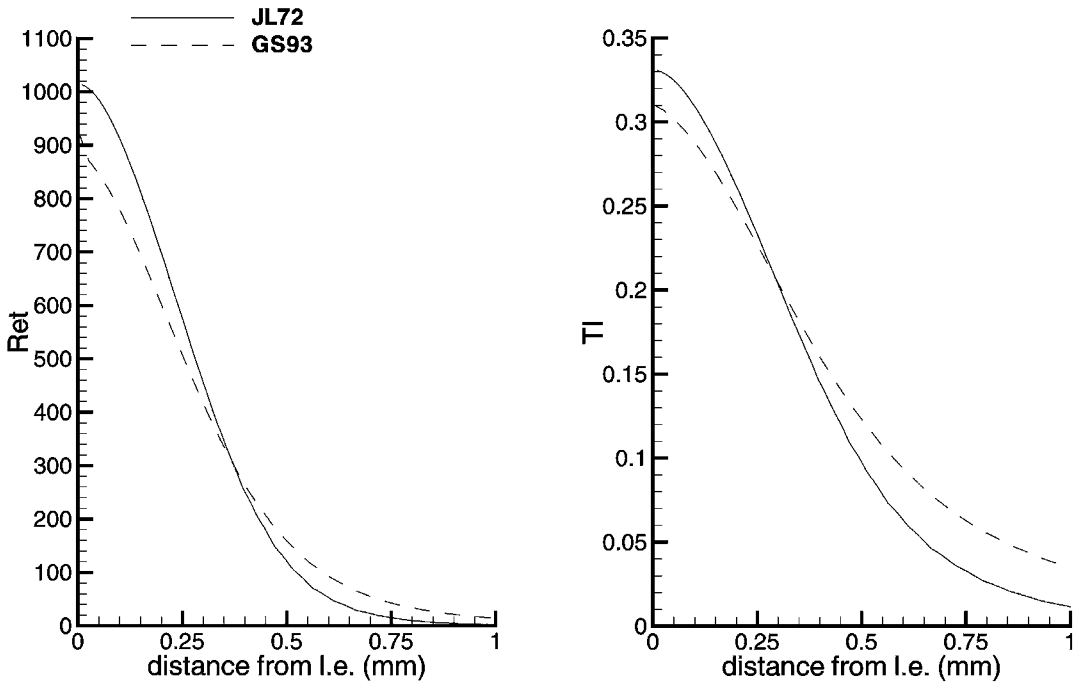

Fig. 32: Turbulence level around the leading edge, profiles along the stagnating streamline
a. Re_t, b. *TI*

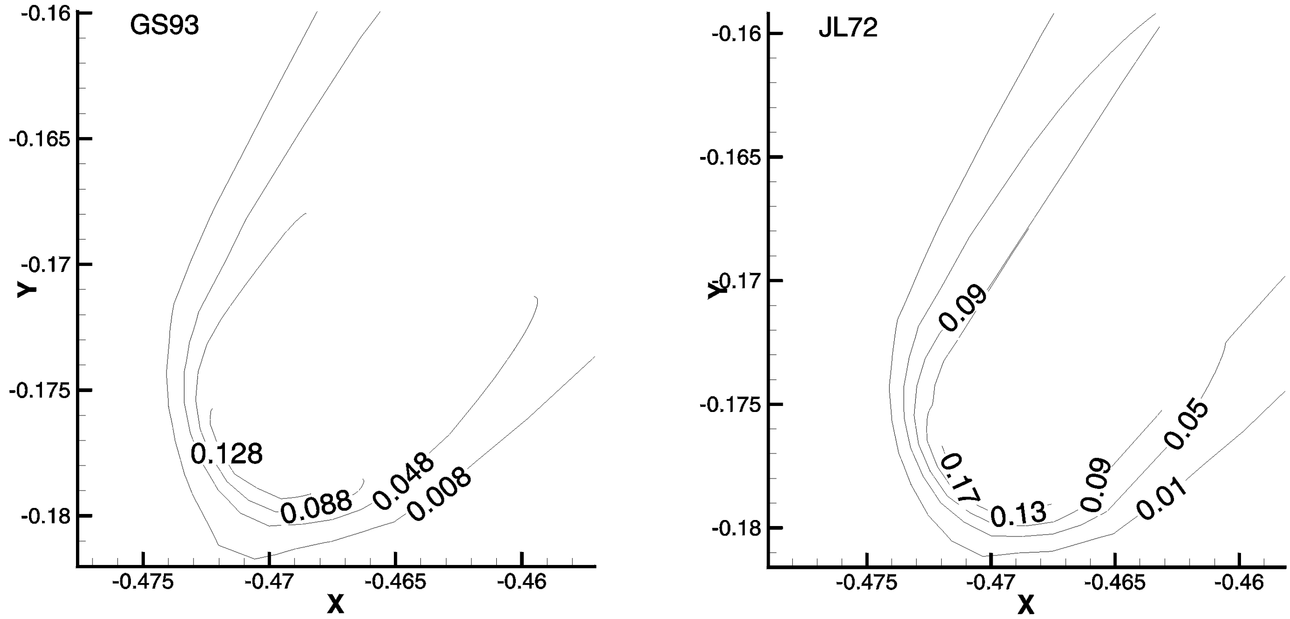

Fig. 33: Turbulence level around the leading edge, turbulence intensity contours